Cross-calibration of the X-ray Instruments onboard the Chandra, Suzaku, Swift, and XMM-Newton Observatories using the SNR 1E 0102.2-7219

Paul P. Plucinsky[a], Andrew P. Beardmore[b], Joseph M. DePasquale[a], Daniel Dewey[c], Adam Foster[a], Frank Haberl[d], Eric D. Miller[c], A.M.T. Pollock[e], Jennifer L.L. Posson-Brown[a], Steve Sembay[b], & Randall K. Smith[a]

[a] Harvard-Smithsonian Center for Astrophysics, MS-70, 60 Garden Street, Cambridge, MA 02138, USA

[b] Department of Physics and Astronomy, University of Leicester, Leicester LE1 7RH, United Kingdom

[c] MIT Kavli Institute for Astrophysics and Space Research, Cambridge, MA 02139, USA

[d] Max-Planck-Institut für Extraterrestrische Physik, Giessenbachstraße , 85748 Garching, Germany

[e] European Space Agency, European Space Astronomy Centre, E-28691 Villanueva de la Cañada, Madrid, Spain

ABSTRACT

We report on our continuing efforts to compare the absolute effective areas of the current generation of CCD instruments onboard the active observatories, specifically: *Chandra* ACIS, *XMM-Newton* EPIC (MOS and pn), *Suzaku* XIS, and *Swift* XRT, using 1E 0102.2-7219, the brightest supernova remnant in the Small Magellanic Cloud. 1E 0102.2-7219 has strong lines of O, Ne, and Mg below 1.5 keV and little Fe emission to complicate the spectrum. The spectrum of 1E 0102.2-7219 has been well-characterized using the RGS grating instrument on *XMM-Newton* and the HETG grating instrument on *Chandra* . We have developed an empirical model that includes Gaussians for the identified lines, an absorption component in the Galaxy, another absorption component in the SMC, and two continuum components with different temperatures. In our fits, the model is highly constrained in that only the normalizations of the four brightest line complexes (the OVII triplet, OVIII Lyα line, the NeIX triplet, and the NeX Lyα) and an overall normalization are allowed to vary, while all other components are fixed. We adopted this approach to provide a straightforward comparison of the measured line fluxes at these four energies. We find that the measured fluxes of the OVII triplet, the OVIII Lyαline, the NeIX triplet, and the NeX Lyαline generally agree to within $\pm$10% for all instruments, with the exception of the OVII triplet and the OVIII Lyαline normalizations for the *Suzaku* XIS1, XIS2, & XIS3, and the *Swift* XRT, which can be up to 20% lower compared to the reference model.

Keywords: instrumentation: detectors — X-rays: individual (E0102)

1. INTRODUCTION

This paper reports the progress of a working group within the *International Astronomical Consortium for High Energy Calibration* (IACHEC) to develop a calibration standard for X-ray astronomy in the bandpass from 0.3 to 2.0 keV. A brief introduction to the IACHEC organization, its objectives, and meetings, may be found at the web page `http://web.mit.edu/iachec/`. Our working group was tasked with selecting celestial sources with line-rich spectra in the 0.3-2.0 keV bandpass which would be suitable cross-calibration targets for the current generation of X-ray observatories. The desire for strong lines in this bandpass stems from the fact that the

Further author information: (Send correspondence to P.P.P.)
P.P.P.: E-mail: plucinsky@cfa.harvard.edu, Telephone: 1 617 496 7726

quantum efficiency and spectral resolution of the current CCD-based instruments changes rapidly with energy from 0.3 to 1.5 keV but the on-board calibration sources currently in use typically have strong lines at only two energies, 1.5 keV (Al Kα) and 5.9 keV (Mn Kα). The only option available to the current generation of flight instruments to calibrate any time variable response is to use celestial sources. The missions which have been represented in this work are the *Chandra X-ray Observatory*[1,2] (*Chandra*), the *X-ray Multimirror Mission*[3] (*XMM-Newton*), the *Suzaku X-ray Observatory* (*Suzaku*), and the *Swift* Gamma-ray Burst Mission. Data from the following instruments have been included in this analysis: the High-Energy Transmission Grating (HETG)[4] and the Advanced CCD Imaging Spectrometer[5–7] (ACIS) on *Chandra* , the Reflection Gratings Spectrometers[8] (RGS), the *European Photon Imaging Camera* (EPIC) Metal-Oxide Semiconductor[9] (MOS) CCDs and the EPIC p-n junction[10] (pn) CCDs on *XMM-Newton* , the X-ray Imaging Spectrometer[39] (XIS) on *Suzaku*, and the X-ray Telescope[11,12] (XRT) on *Swift*.

Suitable calibration targets would need to be constant in time, to have a simple spectrum defined by a few bright lines with a minimum of line-blending, and to be extended so that "pileup" effects in the CCDs are minimized, but not so extended that the off-axis response of the telescope dominates the uncertainties in the response. Our working group focused on supernova remnants (SNRs) with thermal spectra and without a central source such as a pulsar. We narrowed our list to the Galactic SNR Cas-A, the Large Magellanic Cloud remnant N132D and the Small Magellanic Cloud remnant 1E 0102.2-7219 (hereafter E0102). We discarded Cas-A since it is a relatively young ($\sim$ 350 yr) SNR with significant brightness fluctuations in the X-ray, radio, and optical over the past three decades,[13–15] it contains a faint (but apparently constant) central source, and it is relatively large (radius $\sim$ 3.5 arcminutes). We discarded N132D because it has a complicated, irregular morphology in the X-rays[16] and its spectrum shows strong, complex Fe emission.[17] The spectrum of N132D is significantly more complicated in the 0.5–1.0 keV bandpass than the spectrum of E0102. We therefore settled on E0102 as the most suitable source given its relatively uniform morphology, small size (radius $\sim$ 0.4 arcminutes), and comparatively simple X-ray spectrum.

We presented preliminary results from this effort in 2008[18] using a few observations with the calibration available at that time. Here, we present an updated analysis with the latest calibration available at the writing of this paper.

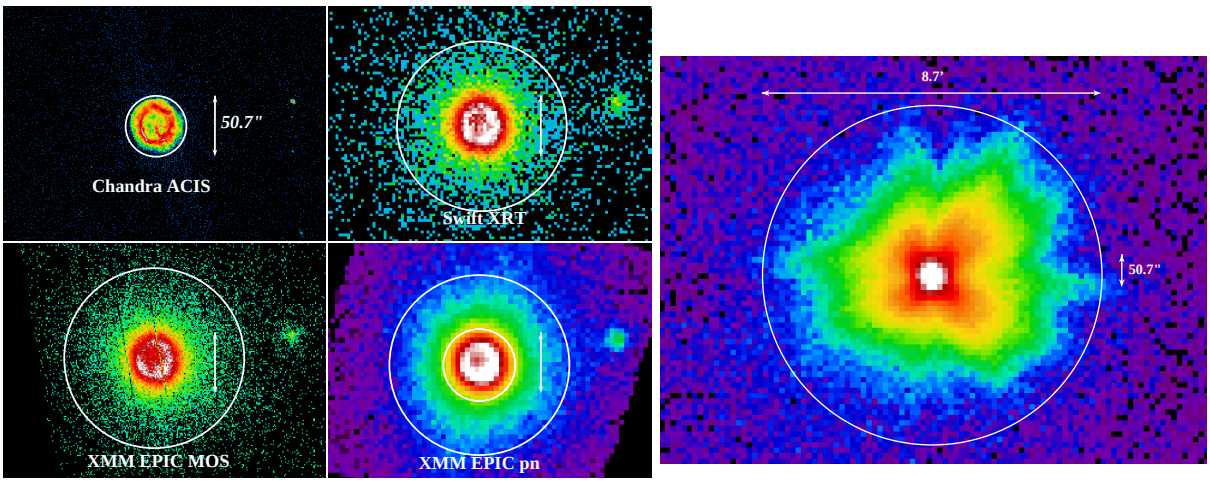

Figure 1. LEFT: Images of E0102 from ACIS S3 (top left), MOS(bottom left), XRT(top right), pn(bottom right). The white circles indicate the extraction regions used for the spectral analysis. The inner white circle on the pn image shows the smaller extraction region that was used for a subset of the observations. RIGHT: Image of E0102 from the *Suzaku* XIS with the extraction region used for the *Suzaku* spectrum.

2. THE SNR 1E 0102.2-7219

1E 0102.2-7219 was discovered by the *Einstein Observatory*.[19] It is the brightest SNR in X-rays in the Small Magellanic Cloud (SMC). E0102 has been extensively imaged by *Chandra* [20,21] and *XMM-Newton* .[22] Figure 1

shows an image of E0102 with the relevant spectral extraction region for each of the instruments included in this analysis. E0102 is classified as an "O-rich" SNR and has an estimated age of $\sim 1,000$ yr. The source diameter is small enough such that a high resolution spectrum may be acquired with the HETG on *Chandra* and the RGS on *XMM-Newton* . The HETG spectrum[23] and the RGS spectrum[24] both show strong lines of O, Ne, and Mg, with little Fe. E0102's spectrum is relatively simple compared to a typical SNR spectrum. Figure 2 displays the RGS spectrum from E0102. The strong, well-separated lines in the energy range 0.5 to 1.5 keV make this source a useful target for calibration observations. The source is extended enough to reduce the effects of photon pileup, which distorts a spectrum. The source is also bright enough to provide a large number of counts in a relatively short observation.

3. SPECTRAL MODELING AND FITTING

3.1 CONSTRUCTION OF THE SPECTRAL MODEL

The development of the spectral model was discussed in detail in our 2008 paper.[18] We summarize the main components of the model below.

We constructed a simple, empirical model based on interstellar absorption components, Gaussians for the line emission, and continuum components which would be appropriate for our limited calibration objectives. We assumed a two-component absorption model using the `tbabs`[25] model in `XSPEC`. The first component was held fixed at 5.36×10^{20} cm^{-2} to account for absorption in the Galaxy. The second component was allowed to vary in total column, but with the abundances fixed to the lower abundances of the SMC.[26–28] We modeled the continuum using a modified version of the `APEC` plasma emission model[29] called the `''No-Line''` model. This model excludes all line emission, while retaining all continuum processes including bremsstrahlung, radiative recombination continua (RRC), and the two-photon continuum from hydrogenic and helium-like ions (from the strictly forbidden $^2S_{1/2}2s \rightarrow$ gnd and $^1S_0 1s2s \rightarrow$ gnd transitions, respectively). The RGS data were adequately fit by a single continuum component with a temperature of kT=0.16 keV, but the HETG, MOS, and pn data showed an excess at energies above 2.0 keV. We therefore added a second continuum component with a temperature of kT=1.74 keV to account for this emission.

The lines were modeled as simple Gaussians in `XSPEC`. The lines were identified in the RGS and HETG data in a hierarchical manner, starting with the brightest lines and working down to the fainter lines. We have used the ATOMDB v1.3.1[30] database to identify the transitions which produce the observed lines. The RGS spectrum from 23 observations totaling 708/680 ks for RGS1/RGS2 is shown in Figure 2 with a linear Y axis to emphasize the brightest lines. The spectrum is dominated by the OVII triplet at 560-574 eV, the OVIII Ly α line at 654 eV, the NeIX triplet at 905-922 eV, and the NeX Lyα at 1022 eV. This figure demonstrates the lack of strong Fe emission in the spectrum of E0102. The identification of the lines obviously becomes more difficult as the lines become weaker. Lines were added to the spectrum at the known energies for the dominant elements – C, N, O, Ne, Mg, Si, S, and Fe.

We included 52 lines in the final model and these lines are described in Table 1 of Plucinsky *et al.* (2008).[18] The absorption and continuum components are described in Table 2 of Plucinsky *et al.* (2008).[18] Our primary purpose is to characterize the flux in the bright lines of O, Ne, and Mg. Any identification of a line with flux less than 1.0×10^{-4} photons cm^{-2} s^{-1} should be considered tentative. The identification of the bright lines is secure, but clarifications are required for the weakest parts of the spectrum, for which our model should be considered an empirical description. For our calibration objective this is not important because the weak lines do not have a significant effect on the fitted parameters of the bright lines of O, Ne, and Mg. We hope that future instruments will have the resolution and sensitivity to uniquely identify the weak lines in the E0102 spectrum.

3.2 FITTING METHODOLOGY

The spectral data were fit using the `XSPEC` software package[31] with the modified Levenberg-Marquardt minimization algorithm and the C statistic[32] as the fitting statistic. The source extraction regions for each of the CCD instruments are shown in Figure 1. Suitable backgrounds were selected for each instrument nearby E0102 where there was no obvious enhancement in the local diffuse emission. We adopted the C statistic to avoid the well-known biases in the χ^2 statistic, though the biases in the case of E0102 are small given how bright the source

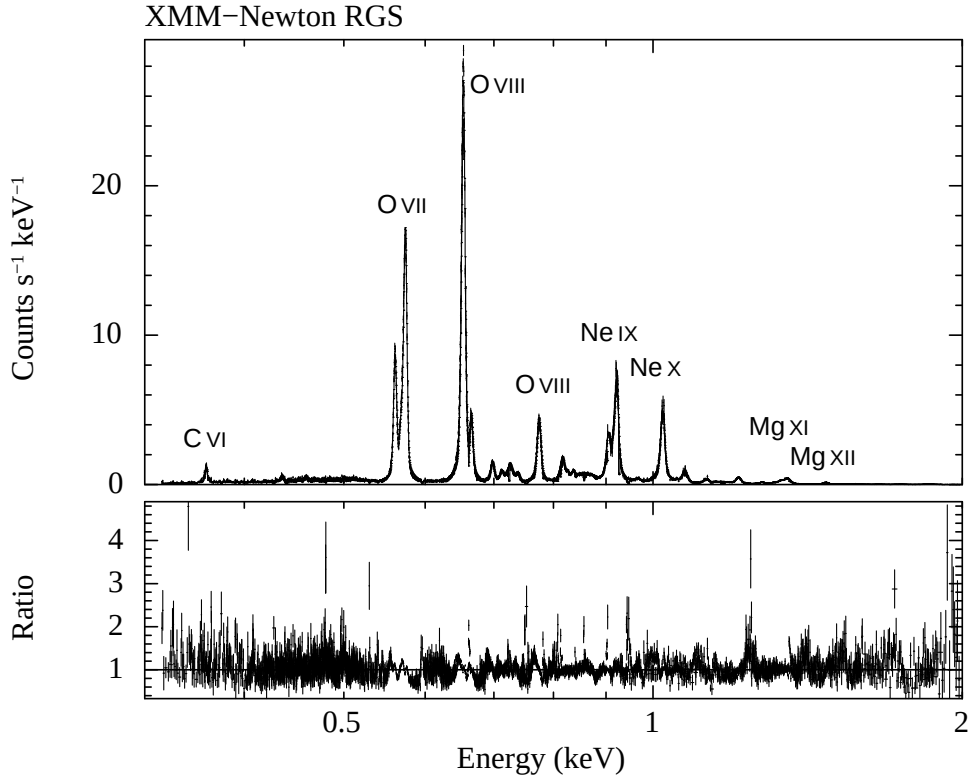

Figure 2. RGS1/2 spectrum of E0102 from a combination of 23 observations. Note the bright lines of O, Ne, and Mg.

is compared to the background. We made use of the feature in `XSPEC` that computes a background model in place of creating an explicit model. We fit the data in the energy range from 0.3 to 2.0 keV (with the exception of the XIS data that were fit in the 0.3–6.0 keV range) since that is the energy range in which E0102 dominates over the background.

Some of the spectral data sets for the various instruments showed evidence of gain variations from one observation to another. Our analysis method is sensitive to small shifts in the gain since our model spectrum has strong, well-separated lines and the line energies are frozen in our fitting process. These small gain shifts (on the order of 5 eV for ACIS and EPIC pn) could be due to a number of factors such as uncertainties in the bias or offset calculation at the beginning of the observation, drifts in the gain of the electronics, or variable particle background. Since our objective is to determine the most accurate normalization for a line at a known energy, it is important that the line be well-fitted. We experimented with allowing the gain to vary for the data sets that showed evidence of a possible gain shift and determined that the fits to the lines improved significantly in some cases. We did not use the `gain fit` command in `XSPEC` in our final analysis because this command shifts the response files instead of shifting the data. The disadvantage of this approach is that the value of the effective area is then evaluated at an incorrect energy and this introduces a systematic error in the determination of the line normalization. This error is small given how small the gain shifts are, nevertheless we adopted the approach of applying the indicated gain shift to the spectral data outside of `XSPEC` and then fitting the modified spectrum to determine the normalization of the line. The ACIS, pn, MOS, & XRT data had gain shifts applied to their data in this manner. The XIS data did not apply a gain shift since no improvement was realized when the gain was allowed to vary.

The number of free parameters needed to be significantly reduced before fitting the CCD data in order to reduce the possible parameter space. In our fits, we have frozen the line energies and widths, the SMC $N_{\rm H}$, and the low-temperature `APEC ‘‘No-Line’’` continuum to the RGS-determined values. The high-temperature `APEC ‘‘No-Line’’` component was frozen at the values determined from the pn and MOS. Since the CCD instruments lack the spectral resolution to resolve lines which are as close to each other as the ones in the OVII triplet and the

NeIX triplet, we treated nearby lines from the same ion as a "line complex" by constraining the ratios of the line normalizations to be those determined by the RGS and by constraining the line energies to the known separations. In practice, we would typically link the normalization and energy of the Forbidden and Intercombination lines of the triplet to the Resonance line. Since we also usually freeze the energies of the lines, this means that the three lines in the triplet would have only one free parameter, the normalization of the Resonance line. In this paper, we focus on adjusting the normalization of the line complexes only. Since most of the power in the spectrum is in the bright line complexes, we froze all the normalizations of the weaker lines. The only normalizations which we allowed to vary were the OVII Res, OVIII Lyαline, the NeIX Res, and the NeX Lyαline normalizations. In addition, we found it useful to introduce a constant scaling factor of the entire model to account for the fact that the extraction regions for the various instruments were not identical. In this manner, we restricted a model with more than 200 parameters to have only 5 free parameters in our fits.

4. OBSERVATIONS

E0102 is routinely observed by *Chandra* , *XMM-Newton* , *Swift* , and *Suzaku* , as a calibration target to monitor the response at energies below 1.5 keV. For the pn we have used all available data in the "small window" mode for this analysis since the results from the individual observations are consistent with each other. For the RGS, we have used all observations in the same readout mode. For ACIS, XIS, and XRT, we have selected a subset of the data from the timeframe and the instrument mode for which we are the most confident in the calibration. We now describe the data processing and calibration issues for each instrument individually.

4.1 XMM-NEWTON RGS

4.1.1 Instruments

The *XMM-Newton* Observatory has two essentially identical high-resolution dispersive grating spectrometers, RGS1 and RGS2, that share telescope mirrors with the EPIC instruments MOS1 and MOS2 and operate between 6 and 38 Å (0.3 and 2.0 keV). The size of its 9 CCD detectors along the Rowland circle define apertures of about 5 arcminutes within which the extended SNR fits comfortably. Each CCD has an image area of 1024×384 pixels, integrated on the chip into bins of 3×3 pixels. The data consist of individual events whose wavelengths are determined by the grating dispersion angles calculated from the spatial positions at which they were detected. Overlapping orders are separated through the event energies assigned by the CCDs. The RGS instruments have suffered the build-up of a contamination layer of carbon, which is corrected for automatically in the calibration. Built-in redundancies have ensured complete spectral coverage despite the loss early in the mission of one CCD detector each in RGS1 and RGS2.

4.1.2 Data

E0102 has been a regular *XMM-Newton* calibration source with 30 observations made at initially irregular intervals and variety of position angles between 2000 April 16 and 2011 November 04. All of these data were used in the RGS analysis reported here, using spectra calculated on a fixed wavelength grid by SAS v11.0.0 separately as normal for RGS1 and RGS2 and for 1st and 2nd orders. An initial set of 23 observations before the end of 2007 was combined using the SAS task `rgscombine` to give spectra of high statistical weight with exposure times of 708080 s for RGS1 and 680290 s for RGS2 and used at an early stage to define the reference model discussed above.

4.1.3 Processing

As E0102 is an extended source, it required special treatment with SAS v11.0.0 whose usual procedures are designed for the analysis of point sources. This simply involved the definition of custom rectangular source and background regions taking into account both the size of the SNR and the cross-dispersion instrumental response caused by scattering from the gratings. In cross-dispersion angle from the SNR center, the source regions were $\pm 0.75'$ and the background regions were between $\pm 1.42'$ and $\pm 2.58'$. An individual measurement was thus encapsulated in a pair of simultaneous spectra, one combining source and background, the other the background only.

Table 1. XMM RGS Observations of E0102

rev	ObsID	DATE-OBS	DATE-END	Exposure(s)
0065	0123110201	2000-04-16T19:08:02	2000-04-17T01:25:43	22661
0065	0123110301	2000-04-17T03:42:14	2000-04-17T09:43:15	21661
0247	0135720601	2001-04-14T20:41:05	2001-04-15T05:59:37	33512
0375	0135720801	2001-12-25T18:00:00	2001-12-26T03:43:39	35019
0433	0135720901	2002-04-20T22:22:05	2002-04-21T08:21:06	35491
0447	0135721001	2002-05-18T10:16:50	2002-05-18T19:45:14	34104
0521	0135721101	2002-10-13T03:19:01	2002-10-13T10:53:05	27244
0552	0135721301	2002-12-14T03:53:17	2002-12-14T11:55:46	28949
0616	0135721401	2003-04-20T12:04:58	2003-04-21T00:42:35	45457
0711	0135721501	2003-10-27T07:54:31	2003-10-27T16:22:24	30473
0721	0135721701	2003-11-16T06:11:25	2003-11-16T13:47:22	27357
0803	0135721901	2004-04-28T07:09:24	2004-04-28T16:56:36	35232
0894	0135722001	2004-10-26T06:56:06	2004-10-26T15:47:57	31911
0900	0135722101	2004-11-06T22:37:30	2004-11-07T12:27:44	49814
0900	0135722201	2004-11-07T13:05:51	2004-11-07T21:57:05	31874
0900	0135722301	2004-11-07T22:35:07	2004-11-08T07:26:29	31882
0981	0135722501	2005-04-17T22:15:21	2005-04-18T08:33:57	37116
1082	0135722601	2005-11-05T06:44:32	2005-11-05T15:11:47	30435
1165	0135722701	2006-04-20T02:24:26	2006-04-20T10:52:27	30481
1265	0412980101	2006-11-05T00:54:41	2006-11-05T09:55:00	32419
1351	0412980201	2007-04-25T12:35:47	2007-04-25T22:42:44	36417
1443	0412980301	2007-10-26T09:48:30	2007-10-26T20:07:08	37118
1531	0412980501	2008-04-19T09:22:15	2008-04-19T17:40:51	29916
1636	0412980701	2008-11-14T19:48:34	2008-11-15T03:50:31	28917
1711	0412980801	2009-04-13T00:04:04	2009-04-13T08:05:57	28913
1807	0412980901	2009-10-21T09:02:24	2009-10-21T17:04:20	28916
1898	0412981001	2010-04-21T01:35:58	2010-04-21T10:04:37	30519
1989	0412981301	2010-10-18T21:40:42	2010-10-19T06:34:18	32016
2081	0412981401	2011-04-20T23:40:43	2011-04-21T09:26:00	35117
2180	0412981501	2011-11-04T09:18:02	2011-11-04T17:41:40	30218

4.2 Chandra HETG

4.2.1 Instruments

The HETG is one of two transmission gratings on *Chandra* which can be inserted into the converging X-ray beam just behind the HRMA. When this is done the resulting HRMA–HETG–ACIS-S configuration is the high-energy transmission grating spectrometer (HETGS, often used interchangeably with just HETG). The HETG and its operation are described as a part of *Chandra*[1,2] and in HETG-specific publications.[4,33]

The HETG consists of two distinct sets of gratings, the medium-energy gratings (MEGs) and the high-energy-gratings (HEGs) each of which produces plus– and minus– order dispersed spectral images with the dispersion angle nearly proportional to the photon wavelength. The result is that a point source produces a non-dispersed "zeroth-order" image (the same as if the HETG were not inserted, though with reduced throughput) as well as four distinct linear spectra forming the four arms of a shallow "X" pattern on the ACIS-S readout; see Figure 1 in Canizares *et al.*(2000).[33]

Hence, an HETG observation yields four first-order spectra, the MEG ±1 orders and the HEG ±1 orders*. Because the dispersed photons are spread out and detected along the ACIS-S, the calibration of the HETG involves more than a single ACIS CCD: the minus side orders fall on ACIS CCDs S2, S1, and S0, while the

*There are also higher-valued orders, $m = 2, 3, \ldots$, but their throughput is much below the first-orders'; the most useful of these are the MEG ±3 and the HEG ±2 orders each with $\sim \times 0.1$ the throughput of the first orders.

Table 2. HETG, ACIS, MOS, XIS, & XRT Observations

OBSID	Instrument	DATE	Exposure(s)[a]	Counts[b] (0.5-2.0 keV)	Mode
120	ACIS-HETG	1999-09-28	87901	38917	TE, Faint, 3.2 s frametime
968	ACIS-HETG	1999-10-08	48414	22566	TE, Faint, 3.2 s frametime
3828	ACIS-HETG	2002-12-20	135914	49599	TE, Faint, 3.2 s frametime
3545	ACIS-S3	2003-08-08	7862.1	57111	TE, 1/4 subarray, 1.1 s frametime
6765	ACIS-S3	2006-03-19	7635.5	51745	TE, 1/4 subarray, 0.8 s frametime
0123110201	MOS1	2000-04-16	17432.3	62131	large win, 0.9s frametime, thin
0123110201	MOS2	2000-04-16	17434.9	60212	large win, 0.9s frametime, thin
0123110301	MOS1	2000-04-17	12087.8	41295	large win, 0.9s frametime, medium
0123110301	MOS2	2000-04-17	12089.4	40619	large win, 0.9s frametime, medium
100044010	XIS0	2005-12-17	59582	97196	full window, 3x3+5x5, SCI=off
100044010	XIS1	2005-12-17	105924	343328	full window, 3x3+5x5, SCI=off
100044010	XIS2	2005-12-17	59586	91092	full window, 3x3+5x5, SCI=off
100044010	XIS3	2005-12-17	59584	81399	full window, 3x3+5x5, SCI=off
00050050004	XRT	2005-02-18	24225	22118	PC mode, combination of 4 obs.
00050050002	XRT	2005-02-23	25287	29423	WT mode, combination of 2 obs.

Notes. [(a)] Exposure for ACIS[-HETG] is "Livetime" (corrected for frame transfer time).
[(b)] Counts for "ACIS-HETG" are the sum of MEG 1 order events, 0.5-2 keV.

plus side orders are on S3, S4, and S5. Hence the calibration of all ACIS-S CCDs is important for the HETG calibration.

4.2.2 Data

E0102 was observed as part of the HETG GTO program at three epochs: Sept.–Oct. 1999 (obsids 120 & 968, t = 1999.75, exp = 88.2+49.0 ks, roll = 11.7°), in December of 2002 (obsid 3828, t = 2002.97, exp = 137.7 ks, roll = 114.0+180°), and most recently in February of 2011 (obsid 12147, t = 2001.11, exp = 150.8 ks, roll = 56.5+180°). The roll angles of these epochs were deliberately chosen to differ with a view toward spectral-tomographic analysis. The HETG view of E0102 is presented in Flanagan *et al.* (2004)[23] using the first epoch observations: the bright ring of E0102 is dispersed and shows multiple ring-like images due to the prominent emission lines in the spectrum. For the limited purpose of fitting the 5-parameter IACHEC calibration model to the HETG data we can collapse the data to 1D and use the standard HETG extraction procedures (next section) along with some modifications to the fitting method.

4.2.3 Processing

The first steps in HETG data analysis are the extraction of 1D spectra and the creation of their corresponding ARFs (as mentioned above, the point-source RMFs are not applicable to E0102.) Because of differences in the pointing of the two first-epoch observations, they are separately analyzed, and so we extract the 4 HETG spectra from each of the 4 obsids available. The archive-retrieved data were processed using *TGCat ISIS* scripts;[34] these provide a useful wrapper to execute the *CIAO* (version 4.4) extraction tools. Because E0102 covers a large range in the cross-dispersion direction compared with the ±16 pixel dither range, we generated for each extraction a set of 7 ARFs spaced to cover the 110 pixels of the cross-dispersion range. Finally, background extractions were made as for the data but with the extraction centers shifted by 120 pixels in the cross-dispersion direction.

The fitting of the HETG extractions generally follows the methodology outlined in Section 3.2 with some adjustments because of the extended nature of E0102, and, secondarily, because of the use of the *ISIS* platform.[35] For each obsid and grating–order we read in the extracted source and background spectra (PHA files) and, after binning, the background counts are subtracted bin-by-bin from the source counts. The corresponding set of ARFs that span E0102's cross-dispersion extent are read in, averaged, and assigned to the data. An RMF that approximates the spatial effects of E0102 is created and assigned as well. Finally the model is defined in ISIS and its 5 free parameters are fit and their confidence ranges determined.

4.3 XMM-Newton EPIC MOS

4.3.1 Instruments

XMM-*Newton*[3] has three X-ray telescopes each with a European Photon Imaging Camera (EPIC) at the focal plane. Two of the cameras have seven MOS CCDs (henceforth MOS1 and MOS2)[9] and the third has twelve pn CCDs (see Section 4.4). Apart from the characteristics of the detectors, the telescopes are differentiated by the fact that the MOS1 and MOS2 telescopes contain the reflection grating arrays which direct approximately half the X-ray flux into the apertures of RGS1 and RGS2.

4.3.2 Data

E0102 was first observed by XMM-*Newton* quite early in the mission in April 2000 (orbit number 0065). The first look at the target was split into two observations, each approximately 18 ksec in duration, with a different choice of optical filter. Observation 0123110201 had the THIN filter and 0123110301 had the MEDIUM filter. Both filters have a 1600 $\mathring{A}$ polyimide film with evaporated layers of 400 $\mathring{A}$ and 800 $\mathring{A}$, respectively, of Aluminum. The EPIC-MOS readout was configured to the Large Window (LW) imaging mode (in the central CCD, only the inner 300×300 pixels of the total available 600×600 pixels are read out). LW mode is the most common imaging mode used in MOS observations of this target as the faster readout (0.9 s compared with 2.6 s in full frame (FF) mode) minimizes pile-up while retaining enough active area to contain the whole remnant for pointings up to around 2 arcminutes from the center of the target. This is useful for exploring the response of the instrument for off-axis angles near to the boresight.

4.3.3 Processing

The MOS data were processed into calibrated event lists with SAS version 11.0.0 and the current calibration files (CCFs) as of May 2012. Source spectra were extracted from a circular region of radius 75 arcseconds centered on the remnant. Background spectra were taken from source-free regions on the same CCD. The event selection filter in the nomenclature of the SAS was (PATTERN==0)&&(#XMMEA_EM). This selects only mono-pixel events and removes events whose reconstructed energy is suspect due, for example, to proximity to known bright pixels or CCD boundaries which can be noisy. Mono-pixel events are chosen over the complete X-ray pattern library because this minimizes the effects of pile-up with little loss of sensitivity over the energy range of interest. The effects of pile-up on the mono-pixel spectrum can be shown to be negligible. The mono-pixel pile-up fraction, the fraction of events lost to higher patterns or formed from two (or more) X-rays detected in the same pixel within a frame (the former is more likely by a factor of about 8:1), can be estimated from the observed fraction of diagonal bi-pixel events which arise almost exclusively from the pile-up of two mono-pixel events. By default the SAS splits these events (nominally pattern classes 26 to 29) back into two separate mono-pixels, although this action can be switched off. Only around 0.7% of events within the source spectra are diagonal bi-pixels which is approximately the same fraction of mono-pixel events lost to horizontal or vertical bi-pixels (event pattern classes 1 to 4). We employ a simple screening algorithm to detect flares in the background due to soft protons. Typically, after this procedure the observed background is less than 1% of the total count rate below 2.0 keV.

All spectra were extracted with a 5.0 eV bin size. Response (RMF) files were generated with the SAS task *rmfgen* in the energy range of interest with an energy bin size of 1.0 eV. Although the source is an extended, but compact, object, the effective area (ARF) file was calculated with the SAS task *arfgen* assuming a point-source function model with the switch PSFMODEL=ELLBETA. We justify this over the computationally more complex procedure of using an external detector map of the remnant to derive a spatially weighted ARF because the variation in vignetting across the remnant is less than 1% and the extraction region used contains greater than 99% of the source encircled energy fraction. The PSMODEL=ELLBETA switch uses the latest 2D model of the PSF. This will become the default in later versions of the SAS.

Shifts in the calibration of the event energy scale were investigated using the *gain fit* command in XSPEC, with an improvement in the fit statistic arising from shifts of around ~ 5 eV at 1.0 keV. This is typical of the calibration accuracy of the event energy scale in the MOS detectors. The values of the parameter normalizations are relatively insensitive to gain shifts of this magnitude. This was confirmed by applying a reverse gain shift, using the values indicated by XSPEC, to the calibrated energies of each event, then re-extracting and re-fitting the spectra.

Table 3. Summary of EPIC pn SW mode observations.

Observation ID	Instrument ID	Date	Exposure (s)	Count Rate[a] counts s^{-1}	Readout Mode
0135720801	PNS001	2001-12-25	21445	12.65 ± 2.4e-02	SW thin filter, centred
0135721101	PNS001	2002-10-13	7180	12.64 ± 4.2e-02	SW thin filter, centred
0135721301	PNS001	2002-12-14	7672	12.60 ± 4.1e-02	SW thin filter, centred
0135721401	PNU002	2003-04-20	8558	12.27 ± 3.8e-02	SW medium filter, centred
0135722401	PNS001	2004-10-14	21447	9.04 ± 2.1e-02	SW thick filter, centred
0135722601	PNS001	2005-11-05	20993	12.23 ± 2.4e-02	SW medium filter, centred
0135722701	PNS001	2006-04-20	21025	12.87 ± 2.5e-02	SW thin filter
0412980101	PNS001	2006-11-05	22382	12.15 ± 2.3e-02	SW medium filter, centred
0412980201	PNS001	2007-04-25	24692	12.82 ± 2.3e-02	SW thin filter
0412980301	PNS001	2007-10-26	25691	12.18 ± 2.2e-02	SW medium filter, centred
0412980501	PNS001	2008-04-19	20627	12.70 ± 2.5e-02	SW thin filter
0412980701	PNS001	2008-11-14	19926	12.37 ± 2.5e-02	SW medium filter
0412980801	PNS001	2009-04-13	14060	12.73 ± 3.0e-02	SW thin filter
0412980901	PNS001	2009-10-21	19946	12.29 ± 2.5e-02	SW medium filter
0412981001	PNS001	2010-04-21	20579	12.80 ± 2.5e-02	SW thin filter
0412981401	PNS001	2011-04-20	23073	12.48 ± 2.3e-02	SW thin filter

Notes. [a] Single-pixel events in the 0.3 − 2.0 keV band.

4.4 XMM-Newton EPIC pn

4.4.1 Instruments

The EPIC pn instrument is based on a back-illuminated 6×6 cm^2 monolithic X-ray CCD array covering the 0.15-12 keV energy band. Four individual quadrants, each having three pn-CCD subunits with a format of 200×64 pixels, are operated in parallel, covering a $\sim 13\farcm6 \times 4\farcm4$ rectangular region. Different CCD-readout modes are available which allow faster readout of restricted CCD areas, with frame times from 73 ms for the full-frame (FF), 48 ms for large-window (LW), and 6 ms for the small window (SW) mode, the fastest imaging mode.[10]

4.4.2 Data

XMM-Newton observed E0102 with EPIC pn in all imaging readout modes (FF, LW and SW) and all available optical blocking filters. To rule out photon pile-up effects, we only used spectra from SW mode data for our analysis. Between 2001-12-25 and 2011-04-20 (satellite revolution 375 to 2081) E0102 was observed by *XMM-Newton* with EPIC-pn in small window (SW) mode 16 times (see Table 3). Only one observation was performed with the thick filter, while for 9 (6) observations the thin (medium) filter was used. One set of observations placed the source at the nominal boresight position which is close to a border of the $4.4' \times 4.4'$ read-out window of pn-CCD 4 and therefore only a relatively small extraction radius of $30''$ is possible. During 8 observations the source was centered in the SW area which allows an extraction with $75''$ radius.

4.4.3 Processing

The data were processed with XMM-SAS version 11.0.1 and we extracted spectra using single-pixel events (PATTERN=0 and FLAG=0) to obtain highest spectral resolution. Response files were generated using `rmfgen` and `arfgen`, assuming a point source for PSF corrections. Due to the extent of E0102, the standard PSF correction for the lost flux outside the extraction region introduces systematic errors, leading to different fluxes from spectra using different extraction radii. To utilize the observations with the target placed at the nominal boresight position, we extracted spectra from the SW-centered observations with $30''$ and $75''$ radius. For the large extraction radius PSF losses are negligible and from a comparison of the two spectra an average correction factor of 1.0315 was derived to account for the PSF losses in the smaller extraction region.

In order to derive reliable line fluxes from the pn spectra, the lines must be at their nominal energies as accurately as possible. Otherwise, the high statistical quality leads to bad fits and wrong line normalizations. Therefore, we created for each observation a set of event files with the energies of the events (the PI value) shifted by up to ±9 eV in steps of 1 eV. In order to do so, the initial event file was produced with an accuracy of 1 eV for the PI values (PI values are stored as integer numbers with an accuracy of 5 eV by default) using the switch testenergywidth=yes in epchain. Spectra were then created from the 19 event files with the standard 5 eV binning. The 19 spectra from each of the SW mode observations were fitted using the model with five free parameters (the overall normalization factor and 4 line normalizations representing the line complexes at O VII, O VIII, Ne IX and Ne X). The best-fit spectrum was then used to obtain the energy adjustment and the line normalizations for each observation.

4.5 Chandra ACIS

4.5.1 Instruments

The ACIS is an X-ray imaging-spectrometer consisting of the ACIS-I and ACIS-S CCD arrays. The imaging capability is unprecedented with a half-power diameter (HPD) of $\sim 1''$ at the on-axis position. We use data from one of the CCDs (ACIS-S3) in the ACIS-S array in this analysis since the majority of imaging data have been collected using this CCD and it has the higher response at low energies than the CCDs in the ACIS-I array. The ACIS-S3 chip is a back-side illuminated device sensitive in the 0.2–10 keV band. The chip has 1024×1024 pixels covering an $8\farcm4 \times 8\farcm4$ area. The spectral resolution is ≈ 150 eV in the 0.3–2.0 keV bandpass.

4.5.2 Data

The majority of the observations of E0102 early in the *Chandra* mission were executed in full-frame mode with 3.2 s exposures. Unfortunately the bright parts of E0102 are significantly piled-up when ACIS is operated in its full-frame mode. In 2005, the *Chandra* calibration team switched to using subarray modes with readout times of 1.1 s and 0.8 s as the default modes to observe E0102, resulting in a reduction in the pileup level. There have been ten subarray observations of E0102, two in node 1 and eight in node 0 of the S3 CCD. We have selected the two earliest OBSIDs for comparison to the other instruments.

4.5.3 Processing

The data were processed with the *Chandra* analysis SW `CIAO` v4.4 and the *Chandra* calibration database CALDB v4.4.10. There are several time-dependent effects which the analysis SW attempts to account for.[36–38] The most important of these is the efficiency correction for the contaminant on the ACIS optical-blocking filter which significantly reduces the efficiency at energies around the O lines. We chose the earliest two OBSIDs to compare to the other instruments since the contamination layer was thinnest at that time. The analysis SW also corrects for the CTI of the BI CCD (S3), including the time-dependence of the gain. Even with this time-dependent gain correction, some of the observations exhibited residuals around the bright lines that appeared to be due to gain issues. We then fit allowing the gain to vary and noticed that some of the observations had significant improvements in the fits when the gain was allowed to adjust. The adjustments were small, about 5 eV, which corresponds to one ADU for S3. These gain adjustments were applied to the spectral data outside of `XSPEC` and then the modified spectra were used for subsequent fits.

4.6 Suzaku XIS

4.6.1 Instruments

The XIS is an X-ray imaging-spectrometer equipped with four X-ray CCDs sensitive in the 0.2–12 keV band. One CCD is a back-side illuminated (XIS1) device and the others are front-side illuminated (XIS0, 2, and 3) devices. The four CCDs are located at the focal plane of four co-aligned X-ray telescopes with a half-power diameter (HPD) of $\sim 2\farcm0$. Each XIS sensor has 1024×1024 pixels and covers a $17\farcm8 \times 17\farcm8$ field of view. The XIS instruments,[39] constructed by MIT Lincoln Laboratories, are very similar in design to the ACIS CCDs aboard *Chandra*.

The XIS2 device suffered a putative micro-meteoroid hit in November 2006 that rendered two-thirds of its imaging area unusable, and it has been turned off since that point. XIS0 also suffered a micro-meteorite hit in

June 2009 that affected one-eighth of the device. Since this region is near the edge of the chip, the device is still used for normal observations, which show no ill effects. The other two CCDs continue to operate normally.

Unlike the ACIS devices, the XIS CCDs possess a charge injection capability whereby a controlled amount of charge can be introduced via a serial register at the top of the array. This injected charge acts to fill CCD traps that cause charge transfer inefficiency (CTI), mitigating the effects of on-orbit radiation damage.[40] In practice, the XIS devices have been operated with spaced-row charge injection (SCI) on since August 2006. A row of fixed charge is injected every 54 rows; the injected row is masked out on-board, slightly reducing the useful detector area.

4.6.2 Data

E0102 is a standard calibration source for Suzaku, with 52 separate observations during the first six years of the mission, including the very first observation when the detector doors were opened. For this work, we have chosen an observation taken shortly after launch on 17 Dec 2005, since this is the longest single observation of E0102 with the XIS (106 ksec of data from the BI device and 60 ksec of data from the FI devices) and it was taken with XIS2 still operational. The observations are summarized in Table 2. Normal, full-window observing mode was employed with charge injection off.

4.6.3 Processing

The data were reprocessed with v2.7 of the XIS pipeline. In particular, the CTI and gain parameters were applied from v20111018 of the `makepi` CALDB file, which reduced the gain uncertainty to less than 5 eV. No further gain correction was applied. As E0102 is only partially resolved by *Suzaku*, spectra were extracted from a 4.35 arcmin radius aperture (the default for a point source), and background spectra were extracted from a surrounding annulus. The redistribution matrix files (RMFs) were produced with the *Suzaku* `FTOOL xisrmfgen` (v20110702), using v20111020 of the CALDB RMF parameters. The ancillary response files (ARFs) were produced with the Monte Carlo ray-tracing `FTOOL xissimarfgen` (v20101105). The ARF includes absorption due to molecular contamination on the optical blocking filter (OBF),[39] using v20091201 of the CALDB contamination parameters. A ring encompassing the bulk of the E0102 emission visible in ACIS images was used as a source image for `xissimarfgen`, however there is little difference between ARFs produced in this way and those produced assuming a simple point source on the sky.

A contaminating point source lies 2 arcmin from E0102, well within the spectral extraction region. This X-ray binary (RXJ0103.6-7201) shows up clearly in ACIS observations, and it is well-modeled by a power law with spectral index 0.9 plus a thermal `mekal` component with kT = 0.15 keV, with a strong correlation between the component normalizations.[41] The emission from this source dominates the extracted spectra above 3 keV; below 2 keV, E0102 thermal emission dominates by several orders of magnitude. We have included the source in our spectral modeling, allowing a single normalization to vary due to the observed source variability. The normalization of the soft thermal component is tied to that of the power law by the best-fit ratio in Haberl *et al.* (2005);[41] the same response products are used to fit this source as E0102, since differences due to vignetting and OBF contamination are accounted for by the variable normalization. Because of the variability of this source, we use a larger energy range of 0.3-6 keV to fit the XIS data. In addition, all four XIS spectra are fit simultaneously, with the normalization of the X-ray binary component tied across all spectra. The individual spectra still have freely varying line normalizations and constant factor, as described in Section 3.2.

4.7 Swift XRT

4.7.1 Instruments

The *Swift* X-ray Telescope (XRT) comprises a Wolter-I telescope, originally built for JET-X, which focuses X-rays onto a CCD detector identical to the type flown on the *XMM-Newton* EPIC-MOS instrument.[11] The CCD, which is responsive to $\sim 0.2-10$ keV X-rays, has dimensions of 600×600 pixels, giving a 23.6×23.6 $arcminute^2$ field. The mirror has a HPD of $\sim$ 18 arcseconds and can provide source localization accurate to better than 2 arcseconds.[42]

Since its launch in 2004 November, *Swift* 's primary science goal has been to rapidly respond to gamma-ray bursts (GRBs) and to achieve this, the XRT was designed to operate autonomously, so that it could measure

GRB light curves and spectra over seven orders of magnitude in flux. In order to mitigate the effects of pile-up, the XRT automatically switches between different CCD readout modes depending on the source brightness. The two most frequently-used modes are: Windowed Timing (WT) mode, which provides 1D spatial information in the central 7.8 arcminutes of the CCD with a time resolution of 1.8 ms, and Photon Counting (PC) mode, which allows full 2D imaging-spectroscopy with a time resolution of 2.5 s.

The CCD charge transfer inefficiency (CTI) was seen to increase approximately threefold a year after launch and has steadily worsened since then. The location and depth of the deepest charge traps responsible for CTI in the central 7.8 arcminutes of the CCD have been monitored since 2007 September and methods have been put in place to minimize their effect on the spectral resolution,[43] though the deepest traps can cause low energy events to be lost below the event threshold ($\sim$ 250 eV).

4.7.2 Data

E0102 is used as a routine calibration source by the XRT, with 20 ks observations taken every 6 to 12 months in both PC and WT modes. The data are used to improve the low energy gain calibration of the CCD, as well as to monitor the degradation in energy resolution below 1 keV. Only observations taken in 2005 are presented here, before deep charge traps had time to form and when the CCD resolution was at its best. An observation summary is shown in Table 2.

4.7.3 Processing

The data were processed with the latest version of the *Swift* software (version 3.9, released 2012-03-12). After the standard screening criteria were applied, total exposures of 24.2 ks for PC mode and 25.3 ks for WT mode were obtained. We selected grade 0 events for the spectral comparison, as this minimizes the effects of pile-up on the PC mode data. (Due to its faster readout, the WT data are free from pile-up.)

A circular region of radius 30 pixels (70.7 arcseconds) was used for the spectral extraction for both modes, though due to the 1D nature of the WT readout this effectively becomes a box of size 60x600 pixels (in detector coordinates) in this mode. Background spectra were selected from suitably sized annular regions. The WT background is $\sim 10\times$ larger than that in PC mode and dominates the WT source spectrum above $\sim$ 3 keV.

For PC mode, exposure corrected ancillary response files were created using the extended source option to the XRTMKARF task. This is not possible for WT mode, so point source corrections were applied — by taking the *Chandra* ACIS image and convolving it with the XRT point spread function, we find the 70.7 arcsecond extraction region contains 95 percent of the SNR encircled energy fraction, which is consistent at the one percent level to that obtained assuming point source corrections apply. The spectra from each obsid were summed while the ancillary response files were averaged, weighted by the per obsid exposure time. The CALDB v011 RMF/ARFs were used, appropriate for data from 2005.

The spectral gain calibration was checked for energy scale offsets in two ways. First, a gain offset fit was performed in XSPEC when the standard model was applied to the data. In the second method, the data were reprocessed applying offsets in 1 eV steps (i.e. a tenth the size of the nominal PI channel width) and the resulting spectra were then fit to find the one which minimized the C-statistic. Both methods gave consistent results, requiring offsets of -1 eV and -5 eV for PC and WT mode, respectively. The gain-corrected spectra were used in the analysis which follows.

5. ANALYSIS & RESULTS

5.1 TIME VARIABILITY

E0102 has an estimated age of 800-1,340 yr based on the expansion study by Hughes *et al.* (2000).[21] It is possible that there might be discernible changes in the integrated X-ray spectrum of an $\sim 1,000$ yr old SNR over a time span of 10 yr. In order to place an upper limit on any changes in the integrated X-ray spectrum, we examined the total count rate from E0102 with the EPIC pn instrument in the 0.3–2.0 keV band. The EPIC pn instrument has proven to be the most stable instrument included in our analysis. In order to eliminate any differences in the calibration of the thin and medium filters, we evaluated the count rates for each instrument/filter combination separately in Table 3. The average count rate of the thin filter data is 12.70 counts s^{-1} with the maximum

difference between the lowest and highest values being 3% of the average. The average count rate of the medium filter data is 12.25 counts s^{-1} with the maximum difference between the lowest and highest values being 1.5% of the average. If we further restrict the comparison to those data acquired at the same location on the detector, indicated by the observations labeled "centered" in Table 3, the difference between the observations narrows significantly. The average count rate of the thin filter, centered data is 12.63 counts s^{-1} with the maximum difference between the lowest and highest values being 0.4% of the average and the average count rate of the medium filter, centered data is 12.21 counts s^{-1} with the maximum difference between the lowest and highest values being 1.0% of the average. We conclude that whatever changes might be occurring in E0102, the effect on the integrated X-ray spectrum is probably 1% or less in the 0.3-2.0 keV band during the time interval of these pn observations.

We also examined the *Chandra* images over a 7.5 yr timeframe to search for small differences within the remnant. The images were exposure-corrected to account for the time-variable absorption of the contamination layer on the ACIS filter and difference images were created with $0\farcs5 \times 0\farcs5$ pixels. We calculated the percentage difference between the two observations in narrow bands around the bright emission line complexes of OVII, OVIII, NeIX, & NeX. The largest differences (pixel to pixel) are on the order of 2%. Some parts of the remnant have apparently brightened while other parts have dimmed. The total flux change is consistent with the value measured with the pn; however we note that the ACIS value has a much larger uncertainty given the relatively large correction that must be applied for the contamination layer.

5.2 SPECTRAL FITS

The spectra for each of the CCD instruments were fit following the description in §3.2. We list the fit statistics, both the C statistic and the χ^2 statistic weighted by the model, in Table 4. None of the fits is formally acceptable in the 0.3-2.0 keV bandpass. However, the quality of the fits is in general quite good around the bright lines of OVII, OVIII, NeIX & NeX with a few exceptions discussed below. The data, model spectra, and residuals are shown in the following figures for each instrument: Figure 4 ACIS, Figure 5 MOS, Figure 6 pn, Figure 7 XIS, and Figure 8 XRT. The ACIS data are well-fitted by the model with the largest deviations occurring around the O lines. The MOS data are well-fitted by the model, resulting in the lowest χ^2 values for any instrument. The pn data are well-fitted by the model with the exception of the OVII triplet. The pattern in the residuals around this line complex indicates that there might be an issue with the spectral redistribution function at the lowest energies. The XIS data are well-fitted by the model, with perhaps some gain differences between the one BI CCD (XIS1) and the other CCDs, which are all FI CCDs. The residuals for the BI CCD are largest at energies below 0.4 keV and above 1.5 keV, indicating perhaps that the XIS1 prefers a different continuum model than the FI CCDs. The XRT PC mode and WT mode fits show a similar pattern in the residuals with the magnitude of the residuals being smaller for the PC mode data. The XRT PC mode data are fit significantly better than the WT mode data, with a reduced χ^2 of 1.69 compared to 3.30.

The fitted values for the five free parameters (overall constant and the line normalizations for the OVII triplet, OVIII Ly α, the NeIX triplet & NeX Ly α) are tabulated in Table 5 along with the 1σ uncertainties. The line normalizations after scaling by the constant are also listed to facilitate comparisons. The overall constant was held fixed to 1.0 for the RGS fits. The values for the MOS in Table 5 are the weighted means of the separate fits to the MOS thin and medium filter observations which are in agreement with each other. These line normalizations are presented in Figure 3 with respect to the IACHEC model values. The line normalizations have been scaled by the overall constant for each instrument and have been plotted relative to the IACHEC standard model value in Figure 3. The constant value is also plotted for reference. A value of 1.0 for a given line normalization means that the line normalization agrees with the IACHEC value, a value of 0.95 means that the normalization is 5% lower than the IACHEC value, a value of 1.05 means that the normalization is 5% higher than the IACHEC value, etc. There are five data points for each instrument, except for the RGS that only has four data points since the constant was fixed at one. The overall constant is the first data point from left to right plotted for that instrument with a color of pink. After this data point, there are four data points from left to right with the following colors, the OVII triplet in black, OVIII Lyαin red, the NeIX triplet in green & NeX Lyαin blue.

There are several interesting trends to note in Figure 3. First, the instruments appear to segregate into two groups, those that appear to be flat with respect to the IACHEC values with energy and those that appear to

Table 4. **Fit Statistics for Data Sets Included in the Comparison**

Instrument	DOF	C Statistic	Reduced χ^2 weighted by model
RGS1	3095	16494.6	5.21
RGS2	2723	15437.9	5.61
HETG	97	-	3.91
ACIS	225	382.4	1.78
MOS1 thin	332	422.7	1.35
MOS1 medium	332	376.9	1.22
MOS2 thin	332	387.8	1.24
MOS2 medium	332	408.7	1.32
pn	337	761.2	2.26
XIS	6227	9960.4	1.52
XRT PC	164	267.0	1.69
XRT WT	164	532.3	3.30

have an energy dependence with the values being lower for the lower energies and higher for the higher energies. The RGS, MOS, pn, ACIS, & XIS0 values appear to be flat with energy compared to the IACHEC values, but the MOS data appear 5-10 % higher, the NeX appears about 5% lower for the pn, the OVIII appears about 10% high for HETG, and XIS0 appears about 5% low except for NeX. The XIS1, XIS2, XIS3, XRT PC and XRT WT all have a similar energy dependence with respect to the IACHEC model with the OVII being the lowest, the OVIII being the next lowest, the NeIX agreeing the best, and the NeX agreeing or perhaps being a little higher than the IACHEC value. We emphasize that the IACHEC model is not being presented as the correct value, rather it is presented as a useful reference to be compared against. The fact that the energy dependence of the differences of the XIS1, XIS2, XIS3, XRT PC and XRT WT values with respect to the IACHEC values are similar is intriguing. This similarity might indicate that a similar correction needs to be applied to the absolute effective area of the XISs and the XRT. Or it might mean that the IACHEC values are biased in energy in some way and the other instruments need a correction to their effective areas. The nature of this discrepancy warrants further investigation. It is also interesting to note that the largest discrepancies occur at the lowest energies for the O lines. If only the NeIX and NeX lines are considered the agreement amongst the instruments is much better, with all instruments agreeing to within ±10%. The fact that the absolute effective area of all of these instruments at 0.9 and 1.0 keV agree to within ±10% is a testament to quality of the calibration for each of these instruments. The larger disagreements at 0.57 and 0.65 keV are most likely related to the complexity of the spectral redistribution function of the various CCDs, the difficulty in measuring the transmission through the filters at these energies, and the uncertainty in the time-variable absorption of the contamination layers for the affected instruments.

As mentioned above, the pn instrument has proven to be the most stable of the instruments included in this study, and we have examined pn data from 2001 until 2011. We have included RGS data from 2000 through 2011 although there are some small trends in the RGS-derived line fluxes with time. All of the other instruments have had significant changes in their response with time that present a challenge to the calibration teams to model accurately. All CCD instruments experience radiation damage in orbit that degrades the spectral resolution of the detector and modifies the redistribution function. ACIS and the XIS also have a time-variable contamination layer that significantly affects the transmission through the filter in this bandpass. The effect of this contamination layer can be seen in Figure 4 in which two ACIS spectra three years apart are overplotted. The decrease in the flux of the O lines is due to the buildup of the contamination layer. Each of the calibration teams has developed models to predict the response of their instruments as a function of time over the course of the mission. We are in the process of comparing these time-dependent models and will report the results in a future paper.

6. CONCLUSION

We have used the line-dominated spectrum of the SNR E0102 to test the response models of the ACIS, MOS, pn, XIS, and XRT CCDs below 1.5 keV. We have fitted the spectra with the same model in which the continuum

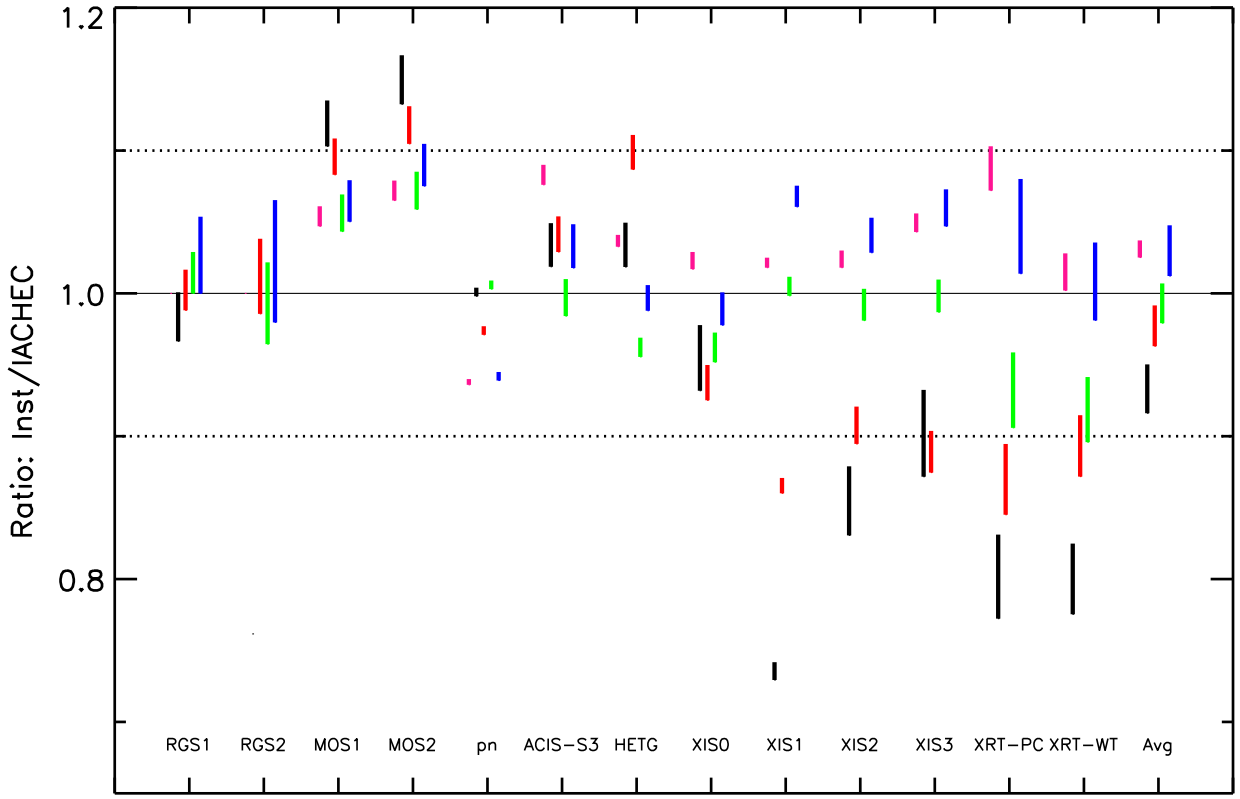

Figure 3. Comparison of the scaled normalizations for each instrument to the IACHEC model values and the average. There are five points for each instrument (except for RGS which only has four) which are from left to right, the overall constant in pink, the OVII line complex in black, the OVIII line in red, the NeIX complex in green, & the NeX line in blue. The length of the line indicates the 1σ uncertainty for the scaled normalization.

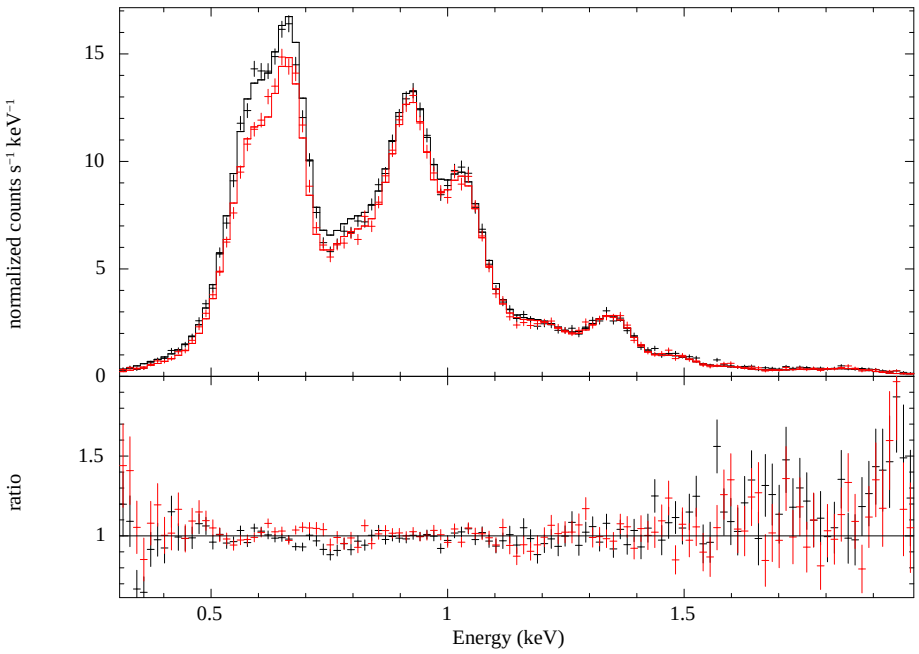

Figure 4. ACIS spectra from OBSIDs 3545(black) & 6765(red) with the best-fitted model and residuals.

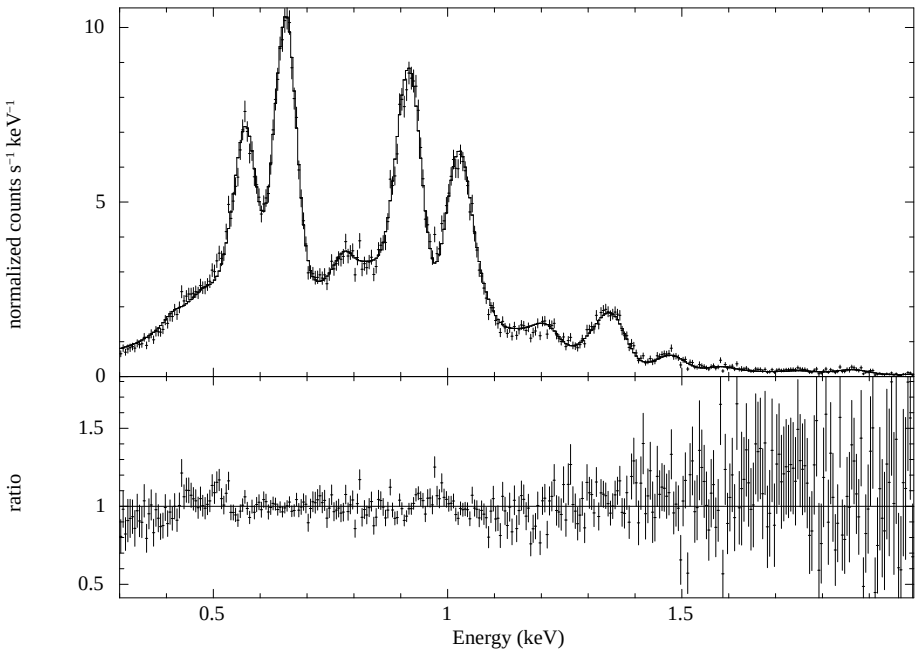

Figure 5. MOS1 spectrum from OBSIDs 0123110201. Note the excellent spectral resolution of the MOS data.

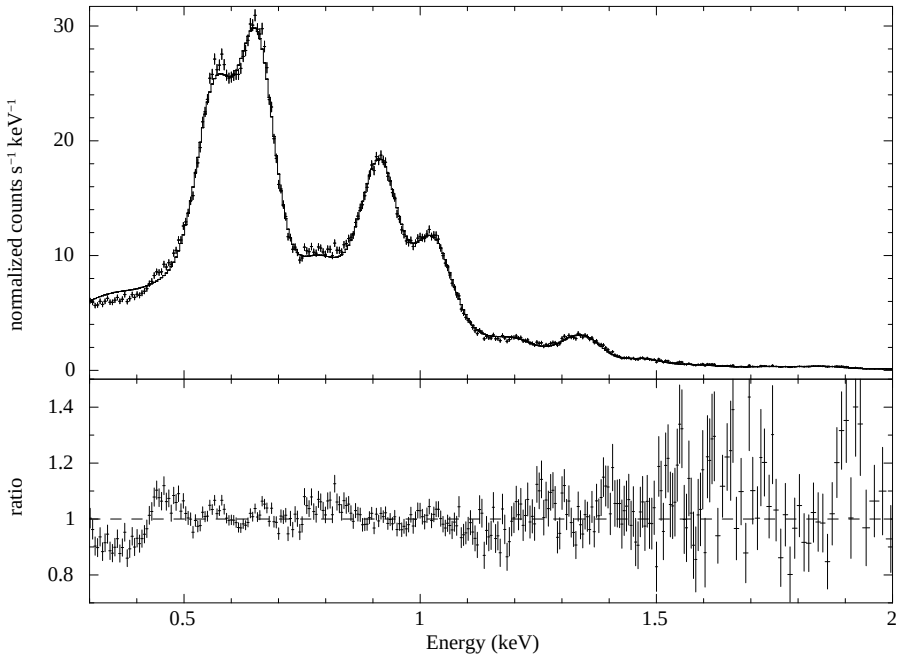

Figure 6. pn spectrum from OBSID0412980301 . Note the high count rate and the pattern in the residuals which might indicate an issue with the spectral redistribution function at the lowest energies.

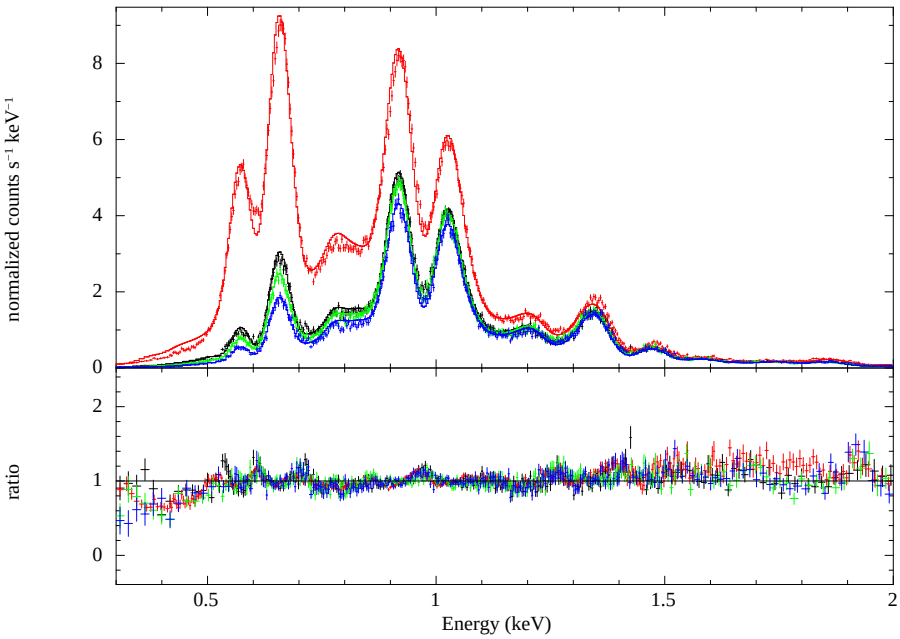

Figure 7. XIS0(black), XIS1(red), XIS2(green), & XIS3(blue) spectra from OBSID 100044010. Note the excellent resolution of the XIS.

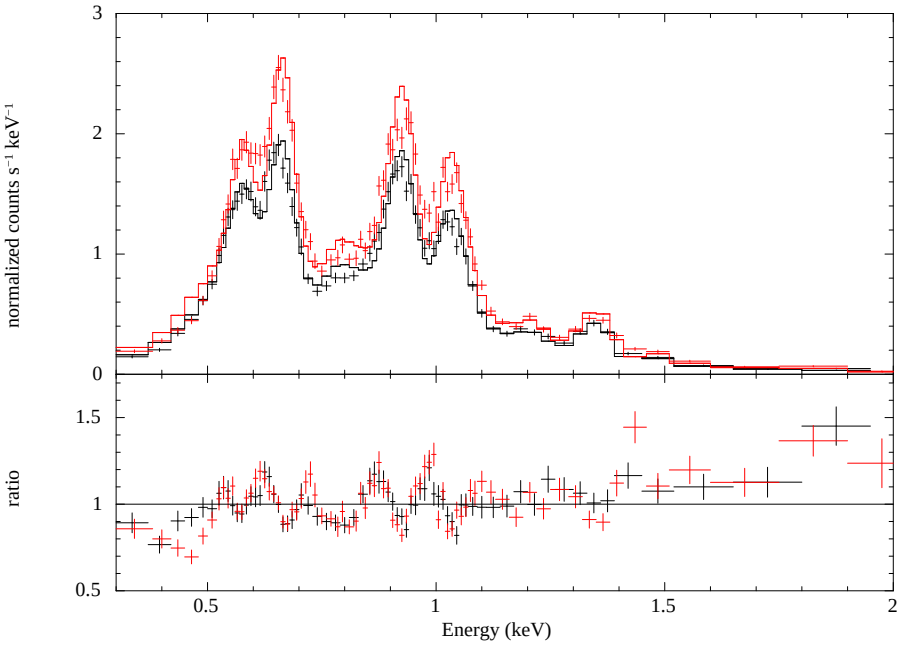

Figure 8. *Swift* XRT spectra from data collected in PC mode (black) and WT mode (red).

Table 5. **Fitted Values for Constant Factor and Line Complex Normalizations**

Instrument	Constant	O VII For Norm (10^{-3}ph cm^{-2}s^{-1})	O VIII Ly α Norm (10^{-3}ph cm^{-2}s^{-1})	Ne IX Res Norm (10^{-3}ph cm^{-2}s^{-1})	Ne X Ly α Norm (10^{-3}ph cm^{-2}s^{-1})
RGS1	1.0	1.292	4.404	1.400	1.415
1σ CL		[1.269,1.314]	[4.341,4.466]	[1.380,1.420]	[1.378,1.452]
Scaled		1.292	4.404	1.400	1.415
RGS2	1.0	no data	4.445	1.371	1.409
1σ CL			[4.330,4.561]	[1.331,1.410]	[1.350,1.468]
Scaled			4.445	1.371	1.409
MOS1	1.054	1.394	4.567	1.383	1.392
1σ CL		[1.374,1.414]	[4.514,4.620]	[1.366,1.400]	[1.373,1.411]
Scaled		1.469	4.814	1.458	1.467
MOS2	1.072	1.408	4.581	1.380	1.401
1σ CL		[1.387,1.429]	[4.527,4.635]	[1.363,1.397]	[1.382,1.420]
Scaled		1.509	4.911	1.479	1.502
pn	0.938	1.401	4.562	1.480	1.384
1σ CL		[1.397,1.405]	[4.548,4.576]	[1.475,1.484]	[1.379,1.388]
Scaled		1.314	4.279	1.388	1.298
ACIS-S3	1.083	1.253	4.224	1.270	1.314
1σ CL		[1.235,1.272]	[4.174,4.275]	[1.254,1.287]	[1.295,1.334]
Scaled		1.357	4.574	1.375	1.423
HETG	1.037	1.309	4.656	1.281	1.325
1σ CL		[1.290,1.329]	[4.604,4.707]	[1.272,1.290]	[1.313,1.337]
Scaled		1.358	4.827	1.328	1.374
XIS0	1.023	1.225	4.026	1.298	1.332
1σ CL		[1.196,1.255]	[3.973,4.079]	[1.284,1.312]	[1.317,1.348]
Scaled		1.253	4.119	1.328	1.363
XIS1	1.022	0.945	3.720	1.357	1.440
1σ CL		[0.937,0.953]	[3.697,3.743]	[1.348,1.366]	[1.430,1.450]
Scaled		0.966	3.802	1.387	1.472
XIS2	1.024	1.096	3.894	1.337	1.400
1σ CL		[1.065,1.127]	[3.838,3.950]	[1.322,1.352]	[1.384,1.417]
Scaled		1.122	3.987	1.369	1.434
XIS3	1.050	1.128	3.720	1.312	1.391
1σ CL		[1.090,1.166]	[3.659,3.781]	[1.297,1.327]	[1.374,1.408]
Scaled		1.184	3.906	1.378	1.460
XRT-PC	1.088	0.967	3.511	1.181	1.325
1σ CL		[0.932,1.003]	[3.412,3.612]	[1.147,1.216]	[1.284,1.368]
Scaled		1.052	3.820	1.285	1.442
XRT-WT	1.015	1.035	3.865	1.249	1.368
1σ CL		[1.003,1.067]	[3.773,3.959]	[1.218,1.280]	[1.332,1.406]
Scaled		1.050	3.923	1.268	1.388

and absorption components and the weak lines are held fixed, while allowing only the normalizations of four bright lines/line complexes to vary. We have compared the fitted line normalizations of the OVII Res line, the OVIII Lyαline, the NeIX Res line, and NeX Lyαline to examine the consistency of the effective area models for the various instruments in the energy ranges around 570 eV, 654 eV, 915 eV, and 1022 eV. We find the largest differences in the derived line fluxes of the OVII and the OVIII line complexes. The largest discrepancy of $\sim 35\%$ exists for the OVII normalization between the XIS1 and MOS2. The largest discrepancy for OVIII is $\sim 25\%$ between the XIS1 and MOS2. The agreement for the Ne lines is much better with all instruments agreeing to within $\pm 10\%$. The differences between the fitted line normalizations and the IACHEC model values show an

apparent energy dependence for the XIS1, XIS2, XIS3, & XRT but a weak or no energy dependence is seen for the RGS, MOS, pn, ACIS, & XIS0.

ACKNOWLEDGMENTS

We thank the members of the IACHEC for their support of this effort, Marcus G. Kirsch, who took a leadership role in setting up this consortium, and Matteo Guainazzi, for guiding the IACHEC over the past several years. This work was supported by NASA contract NAS8-03060.

REFERENCES

[1] Weisskopf, M. C., Tananbaum, H. D., Van Speybroeck, L. P., and O'Dell, S. L., "Chandra x-ray observatory (cxo): overview," in [*X-Ray Optics, Instruments, and Missions III*], Truemper, J. E. and Aschenbach, B., eds., *Proc. SPIE* **4012**, 2 (2000).

[2] Weisskopf, M. C., Brinkman, B., Canizares, C., Garmire, G., Murray, S., and Van Speybroeck, L. P., "An overview of the performance and scientific results from the chandra x-ray observatory," *Publications of the Astronomical Society of the Pacific* **114**, 1 (jan 2002).

[3] Jansen, F., Lumb, D., Altieri, B., Clavel, J., Ehle, M., Erd, C., Gabriel, C., Guainazzi, M., Gondoin, P., Much, R., Munoz, R., Santos, M., Schartel, N., Texier, D., and Vacanti, G., "XMM-Newton observatory. I. The spacecraft and operations," *A&A,* **365**, L1–L6 (Jan. 2001).

[4] Canizares, C. R., Davis, J. E., Dewey, D., Flanagan, K. A., Galton, E. B., Huenemoerder, D. P., Ishibashi, K., Markert, T. H., Marshall, H. L., McGuirk, M., Schattenburg, M. L., Schulz, N. S., Smith, H. I., and Wise, M., "The Chandra High-Energy Transmission Grating: Design, Fabrication, Ground Calibration, and 5 Years in Flight," *PASP* **117**, 1144–1171 (Oct. 2005).

[5] Bautz, M., Pivovaroff, M., Baganoff, F., Isobe, T., Jones, S., Kissel, S., Lamarr, B., Manning, H., Prigozhin, G., Ricker, G., Nousek, J., Grant, C., Nishikida, K., Scholze, F., Thornagel, R., and Ulm, G., "X-ray ccd calibration for the axaf ccd imaging spectrometer," in [*X-Ray Optics, Instruments, and Missions*], Hoover, R. B. and II, A. B. W., eds., *Proc. SPIE* **3444**, 210 (1998).

[6] Garmire, G. P., Bautz, M. W., Ford, P. G., Nousek, J. A., and Ricker, G. R., "Advanced CCD imaging spectrometer (ACIS) instrument on the Chandra X-ray Observatory," in [*X-Ray and Gamma-Ray Telescopes and Instruments for Astronomy*], Truemper, J. and Tananbaum, H., eds., *Proc. SPIE* **4851**, 28–44 (Mar. 2003).

[7] Garmire, G., Ricker, G., Bautz, M., Burke, B., Burrows, D., Collins, S., Doty, J., Gendreau, K., Lumb, D., and Nousek, J., "The axaf ccd imaging spectrometer," in [*American Institute of Aeronautics and Astronautics Conference*], 8 (1992).

[8] den Herder, J. W., Brinkman, A. C., Kahn, S. M., Branduardi-Raymont, G., Thomsen, K., Aarts, H., Audard, M., Bixler, J. V., den Boggende, A. J., Cottam, J., Decker, T., Dubbeldam, L., Erd, C., Goulooze, H., Güdel, M., Guttridge, P., Hailey, C. J., Janabi, K. A., Kaastra, J. S., de Korte, P. A. J., van Leeuwen, B. J., Mauche, C., McCalden, A. J., Mewe, R., Naber, A., Paerels, F. B., Peterson, J. R., Rasmussen, A. P., Rees, K., Sakelliou, I., Sako, M., Spodek, J., Stern, M., Tamura, T., Tandy, J., de Vries, C. P., Welch, S., and Zehnder, A., "The Reflection Grating Spectrometer on board XMM-Newton," *A&A,* **365**, L7–L17 (Jan. 2001).

[9] Turner, M. J. L., Abbey, A., Arnaud, M., Balasini, M., Barbera, M., Belsole, E., Bennie, P. J., Bernard, J. P., Bignami, G. F., Boer, M., Briel, U., Butler, I., Cara, C., Chabaud, C., Cole, R., Collura, A., Conte, M., Cros, A., Denby, M., Dhez, P., Di Coco, G., Dowson, J., Ferrando, P., Ghizzardi, S., Gianotti, F., Goodall, C. V., Gretton, L., Griffiths, R. G., Hainaut, O., Hochedez, J. F., Holland, A. D., Jourdain, E., Kendziorra, E., Lagostina, A., Laine, R., La Palombara, N., Lortholary, M., Lumb, D., Marty, P., Molendi, S., Pigot, C., Poindron, E., Pounds, K. A., Reeves, J. N., Reppin, C., Rothenflug, R., Salvetat, P., Sauvageot, J. L., Schmitt, D., Sembay, S., Short, A. D. T., Spragg, J., Stephen, J., Strüder, L., Tiengo, A., Trifoglio, M., Trümper, J., Vercellone, S., Vigroux, L., Villa, G., Ward, M. J., Whitehead, S., and Zonca, E., "The European Photon Imaging Camera on XMM-Newton: The MOS cameras ," *A&A,* **365**, L27–L35 (Jan. 2001).

[10] Strüder, L., Briel, U., Dennerl, K., Hartmann, R., Kendziorra, E., Meidinger, N., Pfeffermann, E., Reppin, C., Aschenbach, B., Bornemann, W., Bräuninger, H., Burkert, W., Elender, M., Freyberg, M., Haberl, F., Hartner, G., Heuschmann, F., Hippmann, H., Kastelic, E., Kemmer, S., Kettenring, G., Kink, W., Krause, N., Müller, S., Oppitz, A., Pietsch, W., Popp, M., Predehl, P., Read, A., Stephan, K. H., Stötter, D., Trümper, J., Holl, P., Kemmer, J., Soltau, H., Stötter, R., Weber, U., Weichert, U., von Zanthier, C., Carathanassis, D., Lutz, G., Richter, R. H., Solc, P., Böttcher, H., Kuster, M., Staubert, R., Abbey, A., Holland, A., Turner, M., Balasini, M., Bignami, G. F., La Palombara, N., Villa, G., Buttler, W., Gianini, F., Lainé, R., Lumb, D., and Dhez, P., "The European Photon Imaging Camera on XMM-Newton: The pn-CCD camera," *A&A,* **365**, L18–L26 (Jan. 2001).

[11] Burrows, D. N., Hill, J. E., Nousek, J. A., Kennea, J. A., Wells, A., Osborne, J. P., Abbey, A. F., Beardmore, A., Mukerjee, K., Short, A. D. T., Chincarini, G., Campana, S., Citterio, O., Moretti, A., Pagani, C., Tagliaferri, G., Giommi, P., Capalbi, M., Tamburelli, F., Angelini, L., Cusumano, G., Brauninger, H. W., Burkert, W., and Hartner, G. D., "The Swift X-Ray Telescope," *Space Science Reviews* **120**, 165–195 (2005).

[12] Godet, O., Beardmore, A. P., Abbey, A. F., Osborne, J. P., Page, K. L., Tyler, L., Burrows, D. N., Evans, P., Starling, R., Wells, A. A., Angelini, L., Campana, S., Chincarini, G., Citterio, O., Cusamano, G., Giommi, P., Hill, J. E., Kennea, J., LaParola, V., Mangano, V., Mineo, T., Moretti, A., Nousek, J. A., Pagani, C., Perri, M., Capalbi, M., Romano, P., Tagliaferri, G., and Tamburelli, F., "The in-flight spectroscopic performance of the Swift XRT CCD camera during 2006-2007," in [*UV, X-Ray, and Gamma-Ray Space Instrumentation for Astronomy XV. Edited by Siegmund, Oswald H. Proceedings of the SPIE, Volume 6686, pp. 66860A-66860A-8 (2007).*], *Presented at the Society of Photo-Optical Instrumentation Engineers (SPIE) Conference* **6686** (Sept. 2007).

[13] Patnaude, D. J. and Fesen, R. A., "Small-Scale X-Ray Variability in the Cassiopeia A Supernova Remnant," *AJ* **133**, 147–153 (Jan. 2007).

[14] Patnaude, D. J. and Fesen, R. A., "Proper Motions and Brightness Variations of Nonthermal X-ray Filaments in the Cassiopeia A Supernova Remnant," *ApJ* **697**, 535–543 (May 2009).

[15] Patnaude, D. J., Vink, J., Laming, J. M., and Fesen, R. A., "A Decline in the Nonthermal X-ray Emission from Cassiopeia A," *ApJ* **729**, L28 (Mar. 2011).

[16] Borkowski, K. J., Hendrick, S. P., and Reynolds, S. P., "X-Ray-Emitting Ejecta of Supernova Remnant N132D," *ApJ* **671**, L45–L48 (Dec. 2007).

[17] Behar, E., Rasmussen, A. P., Griffiths, R. G., Dennerl, K., Audard, M., Aschenbach, B., and Brinkman, A. C., "High-resolution X-ray spectroscopy and imaging of supernova remnant N132D," *A&A* **365**, L242–L247 (Jan. 2001).

[18] Plucinsky, P. P., Haberl, F., Dewey, D., Beardmore, A. P., DePasquale, J. M., Godet, O., Grinberg, V., Miller, E. D., Pollock, A. M. T., Sembay, S., and Smith, R. K., "The SMC SNR 1E0102.2-7219 as a calibration standard for x-ray astronomy in the 0.3-2.5 keV bandpass," in [*Society of Photo-Optical Instrumentation Engineers (SPIE) Conference Series*], *Society of Photo-Optical Instrumentation Engineers (SPIE) Conference Series* **7011** (Aug. 2008).

[19] Seward, F. D. and Mitchell, M., "X-ray survey of the Small Magellanic Cloud," *ApJ,* **243**, 736–743 (Feb. 1981).

[20] Gaetz, T. J., Butt, Y. M., Edgar, R. J., Eriksen, K. A., Plucinsky, P. P., Schlegel, E. M., and Smith, R. K., "Chandra X-Ray Observatory Arcsecond Imaging of the Young, Oxygen-rich Supernova Remnant 1E 0102.2-7219," *ApJL,* **534**, L47–L50 (May 2000).

[21] Hughes, J. P., Rakowski, C. E., and Decourchelle, A., "Electron Heating and Cosmic Rays at a Supernova Shock from Chandra X-Ray Observations of 1E 0102.2-7219," *ApJL* **543**, L61–L65 (Nov. 2000).

[22] Sasaki, M., Stadlbauer, T. F. X., Haberl, F., Filipović, M. D., and Bennie, P. J., "XMM-Newton EPIC observation of SMC SNR 0102-72.3 EPIC Observation of SMC SNR 0102-72.3," *A&A* **365**, L237–L241 (Jan. 2001).

[23] Flanagan, K. A., Canizares, C. R., Dewey, D., Houck, J. C., Fredericks, A. C., Schattenburg, M. L., Markert, T. H., and Davis, D. S., "Chandra High-Resolution X-Ray Spectrum of Supernova Remnant 1E 0102.2-7219," *ApJ* **605**, 230–246 (Apr. 2004).

[24] Rasmussen, A. P., Behar, E., Kahn, S. M., den Herder, J. W., and van der Heyden, K., "The x-ray spectrum of the supernova remnant 1e 0102.2-7219," *A&A,* **365**, L231 (2001).

[25] Wilms, J., Allen, A., and McCray, R., "On the Absorption of X-Rays in the Interstellar Medium," *ApJ* **542**, 914–924 (Oct. 2000).

[26] Russell, S. C. and Bessell, M. S., "Abundances of the heavy elements in the Magellanic Clouds. I - Metal abundances of F-type supergiants," *ApJS* **70**, 865–898 (Aug. 1989).

[27] Russell, S. C. and Dopita, M. A., "Abundances of the heavy elements in the Magellanic Clouds. II - H II regions and supernova remnants," *ApJS* **74**, 93–128 (Sept. 1990).

[28] Russell, S. C. and Dopita, M. A., "Abundances of the heavy elements in the Magellanic Clouds. III - Interpretation of results," *ApJ* **384**, 508–522 (Jan. 1992).

[29] Smith, R. K., Brickhouse, N. S., Liedahl, D. A., and Raymond, J. C., "Collisional Plasma Models with APEC/APED: Emission-Line Diagnostics of Hydrogen-like and Helium-like Ions," *ApJL* **556**, L91–L95 (Aug. 2001).

[30] Smith, R. and Brickhouse, N., "ATOMDB version 1.3.1," *http://cxc.harvard.edu/atomdb/* (2006).

[31] Arnaud, K., Dorman, B., and Gordon, C., "XSPEC: An X-ray spectral fitting package," *Astrophysics Source Code Library* , 10005 (Oct. 1999).

[32] Cash, W., "Parameter estimation in astronomy through application of the likelihood ratio," *ApJ* **228**, 939–947 (Mar. 1979).

[33] Canizares, C. R., Huenemoerder, D. P., Davis, D. S., Dewey, D., Flanagan, K. A., Houck, J., Markert, T. H., Marshall, H. L., Schattenburg, M. L., Schulz, N. S., Wise, M., Drake, J. J., and Brickhouse, N. S., "High-Resolution X-Ray Spectra of Capella: Initial Results from the Chandra High-Energy Transmission Grating Spectrometer," *ApJ* **539**, L41–L44 (Aug. 2000).

[34] Huenemoerder, D. P., Mitschang, A., Dewey, D., Nowak, M. A., Schulz, N. S., Nichols, J. S., Davis, J. E., Houck, J. C., Marshall, H. L., Noble, M. S., Morgan, D., and Canizares, C. R., "TGCat: The Chandra Transmission Grating Data Catalog and Archive," *AJ* **141**, 129 (Apr. 2011).

[35] Houck, J. C., "ISIS: The Interactive Spectral Interpretation System," in [*High Resolution X-ray Spectroscopy with XMM-Newton and Chandra, Proceedings of the international workshop held at the Mullard Space Science Laboratory of University College London, Holmbury St Mary, Dorking, Surrey, UK, October 24 - 25, 2002, Ed. Branduardi-Raymont, G., published electronically and stored on CD., meeting abstract*], Branduardi-Raymont, G., ed. (Dec. 2002).

[36] Plucinsky, P. P., Schulz, N. S., Marshall, H. L., Grant, C. E., Chartas, G., Sanwal, D., Teter, M., Vikhlinin, A. A., Edgar, R. J., Wise, M. W., Allen, G. E., Virani, S. N., DePasquale, J. M., and Raley, M. T., "Flight spectral response of the ACIS instrument," in [*X-Ray and Gamma-Ray Telescopes and Instruments for Astronomy. Edited by Joachim E. Truemper, Harvey D. Tananbaum. Proceedings of the SPIE, Volume 4851, pp. 89-100 (2003).*], Truemper, J. E. and Tananbaum, H. D., eds., 89–100 (Mar. 2003).

[37] Marshall, H. L., Tennant, A., Grant, C. E., Hitchcock, A. P., O'Dell, S. L., and Plucinsky, P. P., "Composition of the Chandra ACIS contaminant," in [*X-Ray and Gamma-Ray Instrumentation for Astronomy XIII. Edited by Flanagan, Kathryn A.; Siegmund, Oswald H. W. Proceedings of the SPIE, Volume 5165, pp. 497-508 (2004).*], Flanagan, K. A. and Siegmund, O. H. W., eds., 497–508 (Feb. 2004).

[38] DePasquale, J. M., Plucinsky, P. P., Vikhlinin, A. A., Marshall, H. L., Schulz, N. S., and Edgar, R. J., "Verifying the ACIS contamination model with 1E0102.2-7219," in [*Optical and Infrared Detectors for Astronomy. Edited by Garnett, James D.; Beletic, James W. Proceedings of the SPIE, Volume 5501, pp. 328-338 (2004).*], Holland, A. D., ed., 328–338 (Sept. 2004).

[39] Koyama, K., Tsunemi, H., Dotani, T., Bautz, M. . W., Hayashida, K., Tsuru, T. G., Matsumoto, H., Ogawara, Y. ., Ricker, G. R., Doty, J., Kissel, S. E., Foster, R., N akajima, H., Yamaguchi, H., Mori, H., Sakano, M., Hamaguchi, K., Nishiuchi, M., Miyata, E., Torii, K., Namiki, M., Katsuda, S., Matsuura, D., Miyauchi, T., Anabuki, N., Tawa, N., Ozaki, M., Murakami, H., Maeda, Y., Ichikawa, Y., P rigozhin, G. Y., Boughan, E. A., Lamarr, B., Miller, E. D., Burke, B. E., Gregory, J. A., Pillsbury, A., Bamba, A., Hira ga, J. S., Senda, A., Katayama, H., Kitamoto, S., Tsujimoto, M., Kohmura, T., Tsuboi, Y., and Awaki, H., "X-Ray Imaging Spectrometer (XIS) on Board Suzaku," *PASJ* **59**, 23–33 (Jan. 2007).

[40] Ozawa, M., Uchiyama, H., Matsumoto, H., Nakaji ma, H., Koyama, K., Tsuru, T. G., Uchino, M., Uchida, H. an d Hayashida, K., Tsunemi, H., Mori, H., Bamba, A., Ozaki, M., Dotani, T., Kohmura, T., Ishisaki, Y., Murakami, H., Kato, T., Kitazono, T., Kimura, Y., Ogawa, K., Kawai, S. a nd Mori, K., Prigozhin, G., Kissel, S., Miller, E. D., Lama rr, B., and Bautz, M., "Energy-Scale Calibration of the Suzaku X-Ray Imaging Spectrome ter Using the Checker Flag Charge-Injection Technique in Orbit," *PASJ* **61**, 1–+ (Jan. 2009).

[41] Haberl, F. and Pietsch, W., "Discovery of 1323 s pulsations from RX J0103.6-7201: The longest period X-ray pulsar in the SMC," *A&A,* **438**, 211–218 (July 2005).

[42] Evans, P. A., Beardmore, A. P., Page, K. L., Osborne, J. P., O'Brien, P. T., Willingale, R., Starling, R. L. C., Burrows, D. N., Godet, O., Vetere, L., Racusin, J., Goad, M. R., Wiersema, K., Angelini, L., Capalbi, M., Chincarini, G., Gehrels, N., Kennea, J. A., Margutti, R., Morris, D. C., Mountford, C. J., Pagani, C., Perri, M., Romano, P., and Tanvir, N., "Methods and results of an automatic analysis of a complete sample of Swift-XRT observations of GRBs," *MNRAS* **397**, 1177–1201 (Aug. 2009).

[43] Pagani, C., Beardmore, A. P., Abbey, A. F., Mountford, C., Osborne, J. P., Capalbi, M., Perri, M., Angelini, L., Burrows, D. N., Campana, S., Cusumano, G., Evans, P. A., Kennea, J. A., Moretti, A., Page, K. L., and Starling, R. L. C., "Recovering Swift-XRT energy resolution through CCD charge trap mapping," *A&A* **534**, A20 (Oct. 2011).